The Journal of Chemical Physics

The electron shuffle: Cerium influences samarium *4f* orbital occupancy in heteronuclear Ce–Sm oxide clusters

Cite as: J. Chem. Phys. **146**, 194310 (2017); https://doi.org/10.1063/1.4983335
Submitted: 29 March 2017 . Accepted: 29 April 2017 . Published Online: 19 May 2017

Jared O. Kafader, Josey E. Topolski, Vicmarie Marrero-Colon, Srinivasan S. Iyengar, and Caroline Chick Jarrold

The electron shuffle: Cerium influences samarium 4*f* orbital occupancy in heteronuclear Ce–Sm oxide clusters

Jared O. Kafader, Josey E. Topolski, Vicmarie Marrero-Colon, Srinivasan S. Iyengar, and Caroline Chick Jarrold[a)]
Department of Chemistry, Indiana University, 800 East Kirkwood Ave., Bloomington, Indiana 47405, USA

(Received 29 March 2017; accepted 29 April 2017; published online 19 May 2017)

The anion photoelectron (PE) spectra along with supporting results of density functional theory (DFT) calculations on SmO^-, $SmCeO_y^-$, and $Sm_2O_y^-$ ($y = 1, 2$) are reported and compared to previous results on CeO^- [M. Ray *et al.*, J. Chem. Phys. **142**, 064305 (2015)] and $Ce_2O_y^-$ (y = 1, 2) [J. O. Kafader *et al.*, J. Chem. Phys. **145**, 154306 (2016)]. Similar to the results on $Ce_xO_y^-$ clusters, the PE spectra of SmO^-, $SmCeO_y^-$, and $Sm_2O_y^-$ (y = 1, 2) all exhibit electronic transitions to the neutral ground state at approximately 1 eV e^-BE. The Sm centers in SmO and Sm_2O_2 neutrals can be described with the $4f^5 6s$ superconfiguration, which is analogous to CeO and Ce_2O_2 neutrals in which the Ce centers can be described with the $4f$ $6s$ superconfiguration ($Z_{Ce} = Z_{Sm} - 4$). The Sm center in $CeSmO_2$, in contrast, has a $4f^6$ occupancy, while the Ce center maintains the $4f$ $6s$ superconfiguration. The less oxidized Sm centers in both Sm_2O and SmCeO have $4f^6$ $6s$ occupancies. The $4f^6$ subshell occupancy results in relatively weak Sm–O bond strengths. If this extra $4f$ occupancy also occurs in bulk Sm-doped ceria, it may play a role in the enhanced O^{2-} ionic conductivity in Sm-doped ceria. Based on the results of DFT calculations, the heteronuclear Ce–Sm oxides have molecular orbitals that are distinctly localized Sm $4f$, Sm $6s$, Ce $4f$, and Ce $6s$ orbitals. The relative intensity of two electronic bands in the PE spectrum of Sm_2O^- exhibits an unusual photon energy-dependence, and the PE spectrum of $Sm_2O_2^-$ exhibits a photon energy-dependent continuum signal between two electronic transitions. Several explanations, including the high magnetic moment of these suboxide species and the presence of low-lying quasi-bound anion states, are considered. *Published by AIP Publishing.* [http://dx.doi.org/10.1063/1.4983335]

I. INTRODUCTION

Ceria has been rigorously investigated for catalytic applications[1–8] and as an ionically conducting solid electrolyte utilized in solid oxide fuel cells (SOFCs).[9–13] Doped ZnO_2 and ThO_2 have been considered for use in SOFCs, but their high operating temperatures of over 1000 °C[14,15] have made them impractical for large scale production. The ionic conductivity of ceria is increased when doped with samarium, and Sm-doped CeO_2 has proven to be a promising alternative to doped ZnO_2 and ThO_2, with reduced operating temperatures between 400 and 600 °C.[16–18] Lower operating temperatures increase SOFC longevity, decrease the rate of undesired reactions, and allow stainless steel to be implemented in SOFC device interconnections, greatly reducing cost.[19,20] Oxygen vacancies in the fluorite CeO_2 crystal structure introduced from trivalent dopants such as Sm account for the increase in ionic conductivity.[21–24] The optimal dopant concentration of Sm has not been well established, though it is in the range of $x = 0.10$ to 0.20 for $Ce_{1-x}Sm_xO_2$ stoichiometry.[25]

Because bonding in metal oxide systems is localized, cluster models[26,27] of bulk metal oxides can give insight into the local metal-metal interactions in these mixed metal systems that can be complementary to results of studies on bulk systems,[28–33] particularly in efforts to characterize the local features such as defect and dopant sites. In our research program, we have focused on metal oxides in lower-than-traditional oxidation states as models for oxygen vacancies on metal oxide surfaces, which are implicated in some catalytic processes.[8,34–36]

In this report, we compare the previously analyzed photoelectron (PE) spectra of CeO^- and $Ce_2O_y^-$ clusters[37,38] with SmO^-, $Sm_2O_y^-$, and $SmCeO_y^-$ (y = 1–2) clusters. The photoelectron spectra of mixed and pure clusters containing Sm exhibit a large number of transitions to close-lying neutral states resulting from the plethora of close-lying spin states that arise from the nearly half-filled $4f$ subshell in Sm versus the singly occupied $4f$ subshell in Ce. In addition, we find computationally that SmO and SmO^- have two energetically competitive Sm^{2+} and Sm^+ electronic superconfigurations: $4f^6/4f^6 6s$ and $4f^5 6s/4f^5 6s^2$ for the neutral/anion, respectively. The $4f^5 6s/4f^5 6s^2$ electronic structure is determined to be more stable based on the PE spectrum of SmO^- and is analogous to the ligand field favored $4f 6s/4f 6s^2$ superconfigurations for Ce^{2+} and Ce^+ in the CeO/CeO^- diatomics.[39] The same ligand-field favor superconfiguration is found to be favored for Sm_2O_2 and $Sm_2O_2^-$. However, the Sm centers in the less oxidized Sm_2O and SmCeO neutrals and anions, as well as the $SmCeO_2$ neutral and anion, have the more nuclear-shielded $4f^6$ subshell occupation. The lower effective nuclear charge results in a weaker Sm–O bond in these particular heteronuclear and

a)Author to whom correspondence should be addressed. Electronic mail: cjarrold@indiana.edu

profoundly reduced metal oxides. Finally, we consider how the high density of electronic states and potentially high magnetic moment of these samarium oxo clusters may contribute to striking variations in the relative intensities of excited state transitions with photon energy.

II. METHODS

A. Experimental methods

$SmCeO_y^-$ and $SmO^-/Sm_2O_y^-$ PE spectra were collected using an apparatus described in detail previously.[40] $SmCeO_y$ and SmO/Sm_2O_y cluster anions were generated using a laser ablation/pulsed molecular beam valve source.[41] Approximately 3-5 mJ/pulse of the second harmonic (532 nm) output of a Nd:YAG laser, operating at a repetition rate of 30 Hz, was used to ablate the surface of a metal target composed of either compressed Ce/$^{152}Sm_2O_3$ with a 50/50 mol ratio (Alfa-Aesear/Trace Science) or pure $^{152}Sm_2O_3$ powder (Trace Science), respectively. The resulting plasma was entrained by a pulse of ultra-high purity helium buffer gas (40 psig backing pressure) introduced from a solenoid-type molecular beam valve and swept through a 2.5 cm-long, 0.3-cm diameter channel into a vacuum chamber. To hinder clustering and promote the formation of SmO, the 2.5 cm-long channel was removed. After collimation of the gas mixture by a 3-mm skimmer, the anions were accelerated on axis into a 1.2-m beam-modulated time-of-flight mass spectrometer.

Before colliding with a dual microchannel plate ion detector, the anions were selectively photodetached with the second (532.1 nm, 2.330 eV) or third (354.7 nm, 3.495 eV) harmonic output of a second Nd:YAG laser at the intersection of the ion drift tube and a perpendicular 1-m field-free drift tube. The drift times of the small fraction of photoelectrons that traveled the length of the drift tube and collided with a second dual microchannel detector assembly were recorded on a digitizing oscilloscope.

Spectra were accumulated between 380 000 and 1 660 000 laser shots and were measured with laser polarizations parallel ($\theta = 0°$) and perpendicular ($\theta = 90°$) to the electron drift tube with intensities I_0 and I_{90}, respectively, in order to approximate the asymmetry parameter, $\beta(E)$,

$$\beta(E) = \frac{I_0 - I_{90}}{\frac{1}{2}I_0 + I_{90}} \quad (1)$$

which can be related to the symmetry of the molecular orbital associated with electron detachment.

For calibration purposes, the drift times were converted to electron kinetic energy (e^-KE) by identifying common transitions observed in spectra of various Ce-based anions with similar electron affinities (EAs), collected using both photon energies, and setting the difference in the electron kinetic energies (e^-KE) to the fundamental energy (1.1650 ± 0.0001 eV), the difference between the energies of the second and third harmonics, using the relationship,

$$\frac{2(1.1650\ \text{eV})}{m_e} = \left[\frac{\ell}{(t_{3\nu} - t_o)}\right]^2 - \left[\frac{\ell}{(t_{2\nu} - t_o)}\right]^2, \quad (2)$$

where m_e is the electron mass and $t_{3\nu}$ is the drift time of electrons associated with a selected transition observed in the spectrum obtained using 3.49 eV photon energy that can readily be correlated with a transition in the spectrum obtained with 2.33 eV, appearing at $t_{2\nu}$. The equation is solved for ℓ and plotted as a function of t_o. The intersection between this line and other lines generated from several sets of transitions observed in 3.49 eV and 2.33 eV gives a unique ℓ and t_o, the calibration parameters necessary to compute the e^-KE values from electron drift times. The e^-KE values are related to the anion and neutral states via (2) taking into account internal energies for the anion and neutral species,

$$e^-KE = h\nu - EA - T_e^{neutral} + T_e^{anion}. \quad (3)$$

The data presented show electron counts plotted as a function of e^-BE,

$$e^-BE = h\nu - e^-KE. \quad (4)$$

The e^-BE values reflect the energy difference between the final neutral state and the initial anion state and are independent of the photon energy used. Laboratory to center-of-mass frame corrections were made to the e^-KE (and e^-BE) values.

B. Computational methods

Calculations on the molecular and electronic structures of $SmCeO_y^-$, SmO^-, and $Sm_2O_y^-$ anions and neutrals were performed using the unrestricted B3LYP hybrid method within the Gaussian 09 program suite.[42] This method was chosen because it proved to give helpful qualitative insights into CeO and Ce_xO_y anion and neutral species in previous studies.[37,38] In the current study, the same functional and basis sets were used as in the previous studies: To incorporate relativistic effects

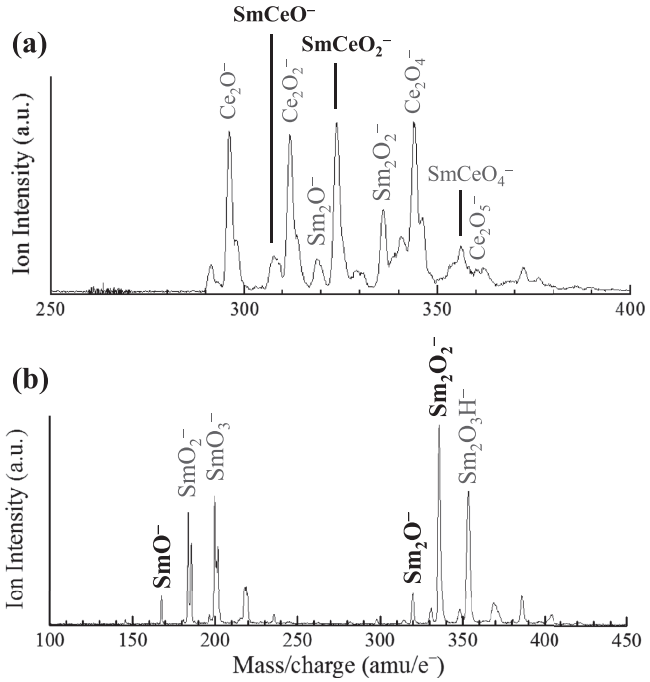

FIG. 1. Mass spectra of cluster anions generated via laser ablation of (a) mixed cerium metal and $^{152}Sm_2O_3$ powder and (b) pure $^{152}Sm_2O_3$ powder. PE spectra are presented for species indicated with bold face.

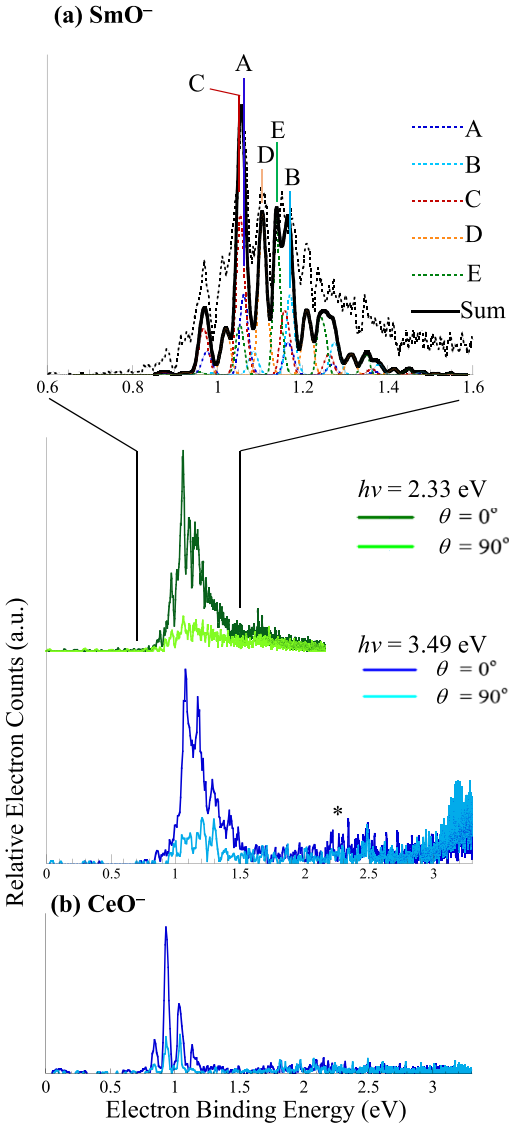

FIG. 2. PE spectrum of (a) SmO^- and (b) CeO^- collected using 2.330 and 3.495 eV photon energies with laser polarizations parallel (dark green and blue traces) and perpendicular (light green and blue traces) to the direction of electron detection. Features indicated with an asterisk (*) are tentatively assigned to shake-up transitions. The simulated transitions A–E (colored dashed lines) and sum (solid black line) are found in the scaled up PE spectrum of SmO^- (dashed black line). See text for details.

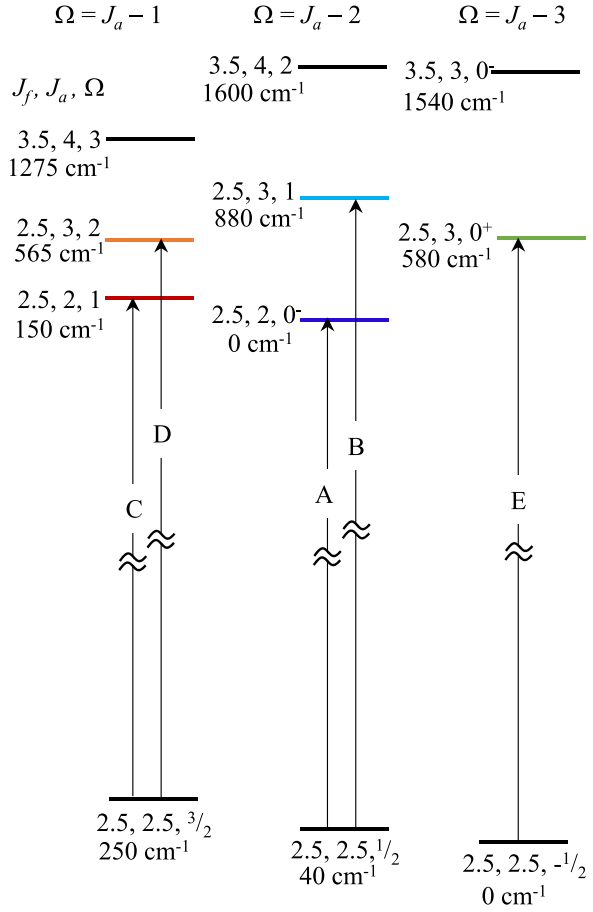

FIG. 3. Schematic correlating of the atomic J_f and J_a values with the molecular Ω values of the transitions contributing to the PES collected from SmO^- [Fig. 2(a)]. The different colored neutral levels represent transitions associated with the simulated spectra of the same color.

on the Ce and Sm metal atoms, the Stuttgart RSC ANO/ECP basis set with 28 core electrons and contraction of (14*s* 13*p* 10*d* 8*f* 6*g*)/[6*s* 6*p* 5*d* 4*f* 3*g*] type, developed by Cao and Dolg, was employed,[43] with the Dunning-style correlation consistent basis set, aug-cc-pVTZ for the oxygen atoms. Geometry optimization and frequency calculations were performed for all the anion and neutral species in multiple spin states. Numerous initial guess structures in a large range of possible spin

TABLE I. Summary of band origin positions in the PE spectrum of SmO^- based on simulated transitions to the known neutral states. The anion and neutral state designations are [J_f, J_a, Ω] associated with the $4f^5$ $6s$ superconfiguration of SmO [Refs. 44 and 45] and the $4f^5$ $6s^2$ superconfiguration of SmO^-. The asymmetry parameter is averaged over the group of overlapping A–E transitions.

	Asymmetry parameter			
Band	$h\nu$ = 2.33 (eV)	$h\nu$ = 3.49 (eV)	e^-BE (eV)	Tentative assignment
C			1.055(3)	[2.5, 2, 1] ← [2.5, 2.5,3/2]
A			1.062(3)	X(0^-) [2.5, 2, 0^-] ← [2.5, 2.5, 1/2]
D	1.2	1.4	1.107(3)	[2.5, 3, 2] ← [2.5, 2.5,3/2]
E			1.142(5)	[2.5, 3, 0^+] ← [2.5, 2.5, (−)1/2]
B			1.173(5)	[2.5, 3, 1] ← [2.5, 2.5, 1/2]
*			2.2–2.6	$5d + e^- \leftarrow 6s^2$ shake-up transition

states were attempted for all anions and neutrals. Higher spin states were considered for clusters containing Sm atoms due to the contribution of more unpaired 4*f* electrons. The supplementary material includes figures presenting all structures that converged for the anions and neutrals, and their relative energies. Adiabatic detachment energies (ADEs) of 1–e^- transitions between anion and neutral states with comparable structures were calculated from the difference between the zero point-corrected energies of the optimized anion and neutral species structures. Photodetachment spectroscopic parameters were gleaned from the optimized anion and neutral structures, vibrational frequencies, and normal coordinates and used to generate simulated spectra using home-written LabView codes for a more quantitative comparison between the experimental and computational results.

TABLE II. Summary of results of DFT calculations on the molecular and electronic structures of SmO/SmO$^-$ including bondlengths and vibrational frequencies. A more extensive catalog of computational results is included in the supplementary material.

Electronic state	Relative energy (eV)	Super configuration	Harmonic frequency (cm^{-1})	Sm–O distance (Å)
SmO				
$^5\Phi$	1.15	$4f^5\,\sigma_{6s}$	822	1.795
$^7\Sigma^+$	0.97	$4f^6$	698	1.894
$^7\Phi$	0.83	$4f^5\sigma_{6s}$	720	1.835
SmO$^-$				
$^8\Sigma^+$	0.46	$4f^6\sigma_{6s}$	630	1.954
$^6\Phi$	0	$4f^5\sigma_{6s}^2$	697	1.849

III. RESULTS

Mass spectra of the $SmCeO_y$ and Sm_xO_y (x = 1–2) anion distributions generated by ablation of the mixed Ce/Sm_2O_3 and pure $^{152}Sm_2O_3$ targets are shown in Figures 1(a) and 1(b), respectively. Fig. 1(a) shows masses assigned to $Ce_2O_y^-$, $SmCeO_y^-$, and $Sm_2O_y^-$ clusters for a range of $y \leq 5$. Fig. 1(b) shows the x = 1 and 2 distributions for the $^{152}Sm_xO_y^-$ clusters, which include several hydroxides. As in our studies on CeO^-, SmO^- could only be made in sufficient quantities under very hot source conditions and with no cooling channel. PE spectra and computational results are presented for the clusters labeled in bold face.

A. SmO^- PE spectrum and computational results

Figure 2(a) shows the PE spectrum of SmO^- obtained with 2.330 eV (green traces) and 3.495 eV photon energies (blue traces) with laser polarization parallel (dark traces) and perpendicular (light traces) to the direction of electron collection. The top panel of Fig. 2(a) shows a portion of the 2.330 eV spectrum on an expanded scale, and the recently reported PE spectrum of CeO^- is included in Fig. 2(b) for comparison.[37] The spectra of SmO^- exhibit a grouping of intense peaks at $e^-BE \approx 1$ eV, in addition to the continuum signal at the high e^-BE edge of the 3.495 eV spectrum consistent with thermionic emission, and a lower intensity group of features between 2.2 eV and 2.6 eV. Similar low-intensity features have been observed in numerous small lanthanide suboxide anion PE spectra, and they are consistent with shake-up transitions associated with promotion of an electron from a diffuse, non-bonding doubly occupied Ln 6*s*-based molecular orbital to an unoccupied but energetically close 5*d*-like orbital in concert with photodetachment of the second electron.[37,38,46]

The more intense set of features around $e^-BE \approx 1$ eV are irregularly spaced. Neutral SmO has 72 electronic states arising from the ligand-field favored Sm^{2+} ($4f^5$ 6*s*) O^{2-} superconfiguration[39] predicted to lie in a 1.5 eV energy range.[44] The X(0^-) ground state is described as [J_f = 2.5, J_a = 2, Ω = 0^-], where J_f is the angular momentum of the $4f^5$ core-like orbital occupancy, $J_a = J_f + j_s$ is the total electronic angular momentum, and Ω, the projection of J_a onto the internuclear axis, which is $J_a - 2$ for the neutral ground state.[45]

Despite the dozens of SmO electronic states that fall within the energy interval of the top panel in Fig. 2(a), most of the partially resolved structure observed in the spectrum can be accounted for by assuming that all of the transitions involve detachment of anions in states with [J_f = 2.5, J_a =

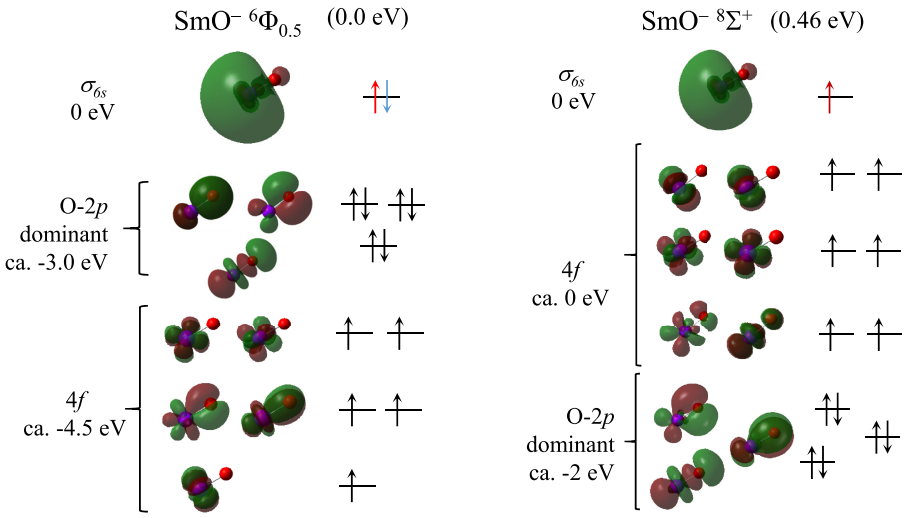

FIG. 4. Lowest energy SmO anion and neutral orbital occupancies. More comprehensive details on relative energies of these and higher energy structures in different spin states are included in the supplementary material. The molecular orbital depictions are labeled with orbital energies relative to the anion HOMO.

2.5, $\Omega'' = J_a - n$ (n = 1, 2, 3)], accessing neutral states with (J_f = 2.5, J_a = 2, 3; $\Omega' = \Omega'' \pm 0.5$). As with the neutral, electronic states of the anion arising from J_f = 3.5 will be approximately 1200 cm^{-1} higher in energy than those arising from J_f = 2.5, with increasing energy as J_a increases to its maximum value of 7.5, and will therefore be less populated than [J_f = 2.5, J_a = 2.5, $\Omega - n$]. The photodetachment transitions involve detachment from the Sm 6*s*-based molecular orbital, so only neutral states with J_f = 2.5 can be observed. Figure 3 shows a simplified schematic of the various neutral states with relative energies organized by how Ω relates to J_a based on the work by Linton *et al.*[45] and Carette and Hocquet.[44] Anions resulting from adding an electron to doubly occupy the Sm 6*s*-like molecular orbital are shown below the associated neutral states.

The simulations shown in the top panel of Fig. 2(a) were done in the following manner. A generic simulation was generated assuming a neutral vibrational frequency of 815 cm^{-1} (close to $\Delta G_{1/2}$ values reported by Linton *et al.*[45]), an anion frequency of 722 cm^{-1}, Δr = 0.04 Å, and T = 2000K for the anion, reflecting the hot source conditions required to generate sufficient quantities of SmO^- (*vide supra*). Two of these generic simulations were added with origins 880 cm^{-1} apart to simulate (A) the transition to the [J_f = 2.5, J_a = 2, Ω = 0^-] neutral ground state and (B) to the [J_f = 2.5, J_a = 3, Ω = 1] partner ($\Delta\Omega = \pm 1/2$), which are the dark and light blue dashed traces, respectively, in Fig. 2(a). The origins are labeled accordingly. The energy between partner transitions to (C) [J_f = 2.5, J_a = 2, Ω = 1] and (D) [J_f = 2.5, J_a = 3, Ω = 2] would be 415 cm^{-1} apart, and the mid-vibrational spacing peak labeled D in the spectrum was well matched assuming transitions (C) and (A) overlapped, which is reasonable since all putative [J_f = 2.5, J_a = 2.5, Ω″] anion states should be close-lying. Based on this, the [J_f = 2.5, J_a = 2.5, Ω = 1.5] state of the anion would be 210 cm^{-1} higher in energy than the [J_f = 2.5, J_a = 2.5, Ω = 0.5] state, as shown in Fig. 3.

Transitions (A)–(D) could be assigned with reasonable confidence because of their consistency with the known neutral state energies.[45] Comparing the four-band simulation with the experimental spectrum revealed one 815-820 cm^{-1} vibrational progression remaining, labeled (E), which by process of elimination is assigned to a transition to the [J_f = 2.5, J_a = 3, $\Omega = 0^+$] neutral state. Given the 580 cm^{-1} neutral term energy, the initial anion state would be the ground state of the anion, lying 40 cm^{-1} lower in energy than the [J_f = 2.5, J_a = 2.5, Ω = 0.5] state. Based on this assignment, the EA of SmO is equal to the band origin of transition (A) plus 40 cm^{-1}, 1.067(6) eV, though we note that 40 cm^{-1} is on the order of our uncertainty in peak position. The band origins and assignments are summarized in Table I.

While the intensities of the transitions are not perfectly matched (the low and unstable anion signal necessitated high detachment powers to collect spectra, resulting in saturation), peak positions align well given the fairly simple approach to the simulation, the main purpose of which was to illustrate that the numerous close-lying anion and neutral states result in a 0.3 eV spread of overlapping transitions.

Results of calculations on SmO^- are consistent with the $4f^5 6s^2$ electron superconfiguration, with a predicted $^6\Phi$ ground state. Results of calculations on the neutral predicted close-lying septet and quintet states arising from the $4f^5 6s$ superconfiguration and lying approximately 1 eV higher in energy than the anion ground state; the calculated EA is 0.83 eV based on the lowest energy $^7\Phi$ state that emerged from the calculations, and the transition to the calculated $^5\Phi$ neutral state 1.15 eV, so the energy spread is in line with the observed 0.3 eV grouping of transitions. These results are summarized in Table II, and the lowest energy orbital occupancy for the anion is shown in Figure 4.

In contrast to the results of our calculations on CeO^- and PrO^-,[37,46] the Sm-local 4*f* orbitals emerge lower in energy than the Sm–O bonding orbitals that arise from O 2*p*–Sm 5*d* overlap, which is evocative of how the energy of the 4*f*

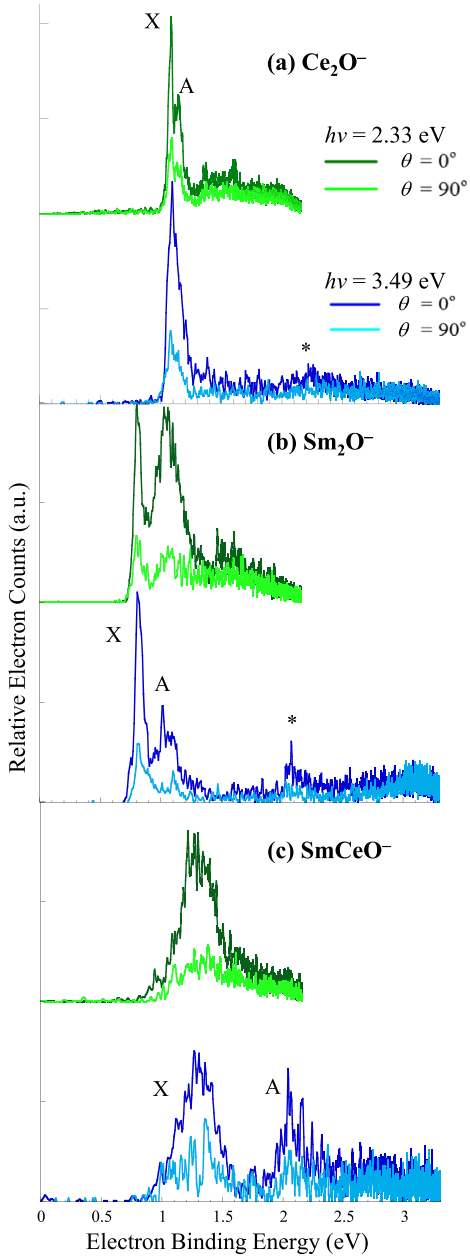

FIG. 5. PE spectra of (a) Ce_2O^-, (b) Sm_2O^-, and (c) $SmCeO^-$ collected using 2.330 and 3.495 eV photon energies with laser polarizations parallel (dark green and blue traces) and perpendicular (light green and blue traces) to the direction of electron detection. Features indicated with an asterisk (*) are tentatively assigned to shake-up transitions.

band in Sm_2O_3 penetrates the valence band.[47,48] We therefore attempted calculations on SmO^- with the $4f^6 6s$ superconfiguration, which converged to an $^8\Sigma^+$ state 0.46 eV higher in energy than the anion ground state. However, the associated $4f^6\ ^7\Sigma^+$ *neutral* was calculated to lie energetically between the $^7\Phi$ and $^5\Phi$ $4f^5 6s$ neutral sates. The $4f^6$ occupancy results in a lower effective nuclear charge on Sm resulting in a weaker Sm–O bond, as evidenced by the lower vibrational frequency and longer bondlength (Table II). A transition between these two states is not observed in the spectrum; it is predicted to lie at approximately 0.5 eV e^-BE. We point out that this superconfiguration is energetically competitive with the $4f^5 6s^2/4f^5 6s$ anion and neutral states because the results on the larger clusters, described next, suggest that the Sm $4f^6$ orbital occupancy becomes more stable in mixed Ce–Sm systems.

B. Sm_2O^- and $CeSmO^-$ PE spectra and computational results

PE spectra of Ce_2O^-, Sm_2O^-, and $CeSmO^-$ are shown in Figures 5(a)–5(c), and transition energies summarized in Table III. Again, the PE spectra were obtained using 2.330 eV (green traces) and 3.495 eV (blue traces) photon energies, and the darker traces represent spectra collected with the laser polarization parallel to the photoelectron drift tube ($\theta = 0°$) and the lighter traces represent spectra taken with perpendicular polarization ($\theta = 90°$).

As described previously, the PE spectrum of Ce_2O^- exhibits two close-lying and narrow transitions labeled X and A in Fig. 5(a),[38] with the first excited state transition exhibiting a slightly more extended vibrational progression in a low-frequency mode. The Sm_2O^- spectrum [Fig 5(b)] obtained with 3.495 eV photon energy is qualitatively similar, though band X is 0.35 eV lower in energy than band X in the Ce_2O^- spectrum, and bands X and A are more distinctly resolved. There is additionally a feature similar to the shake-up features observed in other lanthanide oxide spectra (*vide supra*) labeled with an asterisk (*). The relative intensity of band A to band X in the Sm_2O^- spectrum obtained using 2.330 eV photon energy is distinctly higher than the relative intensities in the 3.495 eV spectrum. Similar enhancements are observed in several other mixed Ce–Sm and pure Sm oxide spectra. Possible explanations will be considered in Sec. IV.

The spectrum of $CeSmO^-$ [Fig. 5(c)] is very different, exhibiting two vibrationally extended transitions at e^-BE values of approximately 1.0 and 2.0 eV, labeled X and A, respectively. Band X, which is 0.5 eV full width at half maximum (FWHM), exhibits a 670 cm^{-1} progression of partially resolved shoulders, which is readily reconciled with results of calculations (*vide infra*).

The lowest energy structures found computationally for both Sm_2O and CeSmO anions and neutrals are O-atom bridge bonded structures, as summarized in Figures 6 and 7, respectively. O–M–M′ structures converged at least 1 eV higher in energy; these structures and energies are included in the supplementary material.

The lowest energy state found for Sm_2O^- is a $^{14}B_2$ obtuse C_{2v} structure with 12 unpaired electrons in the 14 $4f$-local orbitals and three electrons in Sm $6s$-based molecular orbitals: $[4f_a^6\ 4f_b^6](\sigma_{6s})^2(\sigma^*_{6s})$, where a and b represent the two different Sm centers. Note that we refer to the a_1 orbital that is the in-phase combination of the $6s$ orbitals on the two Sm centers as σ_{6s}, and the associated out-of-phase b_2 orbital as σ^*_{6s}, because it allows direct comparison with nearly identical MO's of the other species. This electronic structure is qualitatively different from the lowest energy Ce_2O^- structure in that, relative to their respective atomic numbers, the Sm centers have an additional electron in the $4f$ subshell. The electronic structure of Sm_2O^- that would be analogous to Ce_2O^- would be a 12-tet state described as $[4f_a^5\ 4f_b^5](\sigma_{6s})^2(\sigma_{5d}\text{ or }\pi_{5d})(\sigma^*_{6s})^2$. The lowest energy neutral found is a near linear 15-tet state (symmetry unrecognized by the electronic structure code; we refer to it as the $^{15}A'$ state) accessed by detachment of an electron from the weakly bonding (σ_{6s}) HOMO−1 orbital, resulting in the $[4f_a^6\ 4f_b^6](\sigma_{6s})(\sigma^*_{6s})$ orbital occupancy. Detaching an electron from the singly occupied (σ^*_{6s}) HOMO of the anion results in the $^{13}A_1$ neutral with a smaller bond angle. The two

TABLE III. Peak positions and tentative assignments for the PE spectra of Ce_2O^-, Sm_2O^-, and $SmCeO^-$ [Fig. 5]. The values in parentheses represent the uncertainty in the last digit. The uncertainty in the asymmetry parameters is approximately 10%.

	Asymmetry parameter			
	$h\nu$ = 2.33 (eV)	$h\nu$ = 3.49 (eV)	ADE/VDE e^-BE (eV)	Tentative assignment
Ce_2O^-				
X	1.0	1	1.06(2)/1.09(2)	$^5A_1 \leftarrow {}^4B_2$ or $^5B_1 \leftarrow {}^4A_2$
A	0.9	1.2	VDE = 1.16(2)	$^3A_1 \leftarrow {}^4B_2$ or $^3B_1 \leftarrow {}^4A_2$
*	···		VDE = 2.3(1)	Shake-up transition
Sm_2O^-				
X	0.8	1	0.71(1)/0.801(6)	$^{15}A' \leftarrow {}^{14}B_2$
A	1.0	1.4	VDE = 1.06(3)	$^{13}A_1 \leftarrow {}^{14}B_2$
*	···		VDE = 2.078(5)	Shake-up transition
$SmCeO^-$				
X	1.0	1.3	0.80(2)/1.218(4)	$^9A' \leftarrow {}^8A'$ and $^7A' \leftarrow {}^8A'$
A	0.9	···	VDE = 2.042(6)	

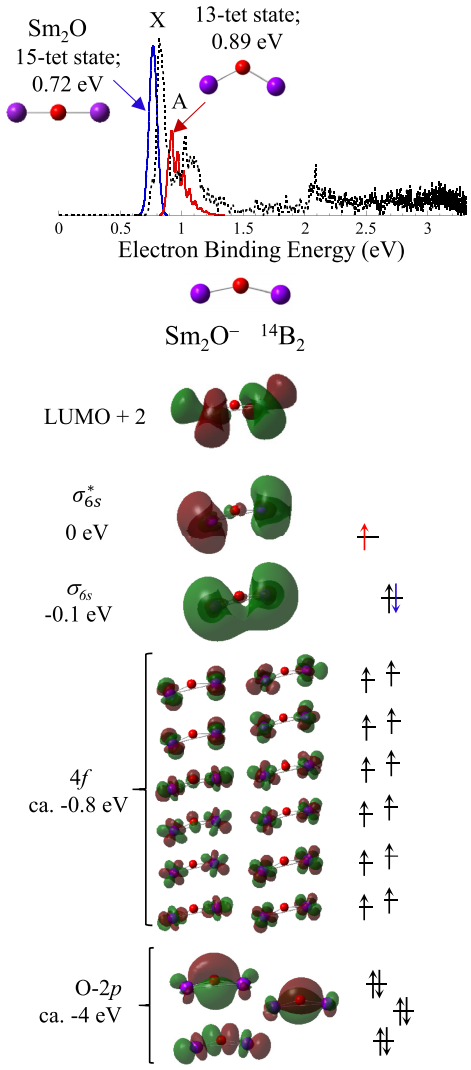

FIG. 6. Summary of the lowest energy structure and spin state that converged in calculations on Sm_2O^- and Sm_2O, along with the orbital occupancy of the lowest energy state found for Sm_2O^-. Simulations (solid blue and red traces) of the Sm_2O^- PE spectrum (dashed black trace). The simulations are color-coordinated with the detached electrons.

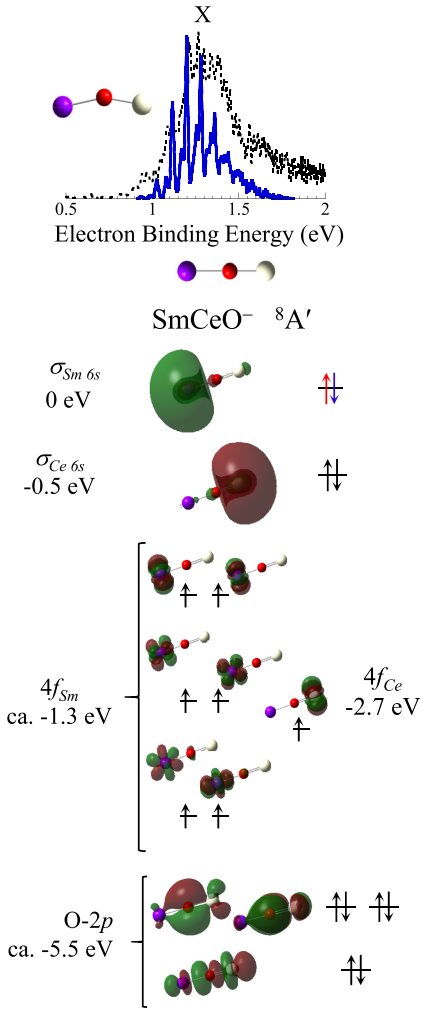

FIG. 7. Summary of the lowest energy structure and spin state that converged in calculations on $SmCeO^-$, along with the orbital occupancy of the lowest energy electronic state. Simulation (solid blue trace) of the $SmCeO^-$ PE spectrum (dashed black trace) is based on the transition associated with detachment of the Sm-local 6*s*-like MO resulting in the higher spin neutral state. Transitions to the lower-spin neutral state are predicted to overlap with this transition.

TABLE IV. Summary of results of DFT calculations on the molecular and electronic structures of Sm_2O/Sm_2O^- and $SmCeO/SmCeO^-$ including bondlengths, angles, and vibrational frequencies. A more extensive catalog of computational results is included in the supplementary material.

Electronic state	Relative energy (eV)	Super-configuration	Allowed transitions	Symmetric mode frequency (cm^{-1})	Sm–O (Å)// ∠(Sm–O–Sm)
Sm_2O				Bend/sym. str/asym. str	
$^{11}A'$	1.03	$4f^{12}\sigma_{6s}\sigma^*_{6s}$	$^{13}A' \leftarrow {}^{12}B_2$ (0.78 eV)	76/168/624	2.103//~180°
$^{13}A_1$	0.89	$4f^{12}\sigma^2_{6s} + e^-$	$^{13}A' \leftarrow {}^{14}B_2$ (0.89 eV)	67/392/540	2.097//124°
$^{15}A'$	0.72	$4f^{12}\sigma_{6s}\sigma^*_{6s}$	$^{15}A' \leftarrow {}^{14}B_2$ (0.72 eV)	82/171/668	2.111//~180°
Sm_2O^-					
$^{12}B_2$	0.11	$4f^{12}\sigma^2_{6s}\sigma^*_{6s}$		48/212/445	2.104//159°
$^{2}A'$	0.05	$4f^{12}\sigma^2_{6s}\sigma^*_{6s}$		46/215/513	2.107/2.108//158°
$^{14}B_2$	0	$4f^{12}\sigma^2_{6s}\sigma^*_{6s}$		47/229/566	2.110//155°
SmCeO				Bend/Ce–Sm/O-stretch	*M*–O (Sm/Ce)/Å//∠(Sm–O–Ce)
$^{7}A'$	1.14	$4f^6_{Sm}4f_{Ce}6s^2_{Ce}6s_{Sm}$	$^{7}A' \leftarrow {}^{8}A'$ (1.14 eV)	25/252/653	2.232/1.936//144°
$^{9}A'$	1.02	$4f^6_{Sm}4f_{Ce}6s^2_{Ce}6s_{Sm}$	$^{9}A' \leftarrow {}^{8}A'$ (1.02 eV)	10/229/675	2.214/1.945//154°
$SmCeO^-$					
$^{8}A'$	0	$4f^6_{Sm}4f_{Ce}6s^2_{Ce}6s^2_{Sm}$		55/147/733	2.318/1.923//180°

neutral states are calculated to be very close-lying, which reflects how the bond and anti-bond formed by the two Sm 6*s*-like orbitals have very little bonding character. A simulation based on the anion and neutral structures is shown in the top panel of Fig. 6. The origins of the two transitions are set to the calculated ADE values, though the intensity of the $^{13}A_1$ – $^{14}B_2$ transition was scaled by 0.5. The agreement between the simulated and experimental spectra is good.

Table IV also includes the energies of low-lying anions in different spin states. Of note is the $^2A'$ anion (symmetry not identified in the calculations) calculated to be 0.05 eV higher in energy than the ground $^{14}B_2$ state, suggesting that ferromagnetic and antiferromagnetic (AF) spin states are close in energy. However, neutrals with AF spin states converged much higher in energy than their ferromagnetic analogs.

With $SmCeO^-$, disparate subshell energies for the two metal centers are predicted to result in a more striking localization of Sm 4*f*, Sm 6*s*, Ce 4*f*, and Ce 6*s* orbitals, as shown in Fig. 7. The lowest energy anion that converged is $^8A'$, which can be described generally as having $[4f^6_{Sm}4f_{Ce}](6s_{Ce})^2(6s_{Sm})^2$ orbital occupancy. Again, the Sm center has six electrons in the 4*f* subshell, in contrast to five in the SmO diatomic ground state. Detachment of an electron from the $6s_{Sm}$ HOMO results in the nonet or septet neutral state with $[4f^6_{Sm}4f_{Ce}](6s_{Ce})^2(6s_{Sm})$ occupancy, with the septet state predicted to be 0.12 eV higher in energy. Given the systematic overestimation of exchange with the method used, the true energies are anticipated to be closer in energy, and transitions to the two spin states should be overlapping within this band that is 0.4 eV wide FWHM.

The bondlengths predicted for $SmCeO^-$ and SmCeO reflect the effect of the Sm $4f^6$ subshell occupancy. The Sm–O bondlengths for the anion and two neutral states are predicted to be 2.2–2.3 Å, while the Ce–O bondlengths are 1.92–1.95 Å. The "extra" 4*f* orbital occupancy on the Sm center results in more nuclear shielding, and the Sm–O ionic bond is consequently weaker than the Ce–O ionic bond.

A simulation of the $^9A'$–$^8A'$ transition based on the calculated spectroscopic parameters is shown in the top panel of Fig. 7. The simulated peaks coincide with the pattern of lines, though there are peaks in the experimental spectrum lying between the peaks of the predicted 674 cm^{-1} stretch progression, supporting the suggestion that transitions to these two neutral states are overlapping and on the order of 0.05 eV apart.

We would also anticipate that detachment transitions involving the Ce-local 6*s* orbital would be observed in the PE spectrum and suggest that band A is due to transitions to the $[4f^6_{Sm}4f_{Ce}](6s_{Ce})(6s_{Sm})^2$ neutral nonet and septet states.

C. Sm_2O_2 and $SmCeO_2$ PE spectra and computational results

PE spectra of $Ce_2O_2^-$, $Sm_2O_2^-$, and $SmCeO_2^-$ are shown in Figures 8(a)–8(c), respectively, with transition energies summarized in Table V. As previously described, the PE spectrum of $Ce_2O_2^-$ is composed of two narrow and comparably intense bands X and A, which appear to have overlapping close-lying near-vertical transitions from different initial spin states of the anion.[38] The spectrum of $Sm_2O_2^-$ has two much broader transitions at e^-BE values 0.70(1) eV and 1.58(1) eV, labeled X and (*), the latter being significantly lower in intensity than band X. We note here that band X in the spectrum of $Sm_2O_2^-$ is broader than, but comparable to, the group of five overlapping transitions in the SmO^- spectrum. Based on the calculations presented below, we believe that there are two transitions correlating to bands X and A in the $Ce_2O_2^-$ PE spectrum that are congested by more close-lying electronic states arising from a single superconfiguration in $Sm_2O_2^-$. As illustrated in Figs. 8(a) and 8(b), the X–A splitting in the $Ce_2O_2^-$ spectrum falls well within

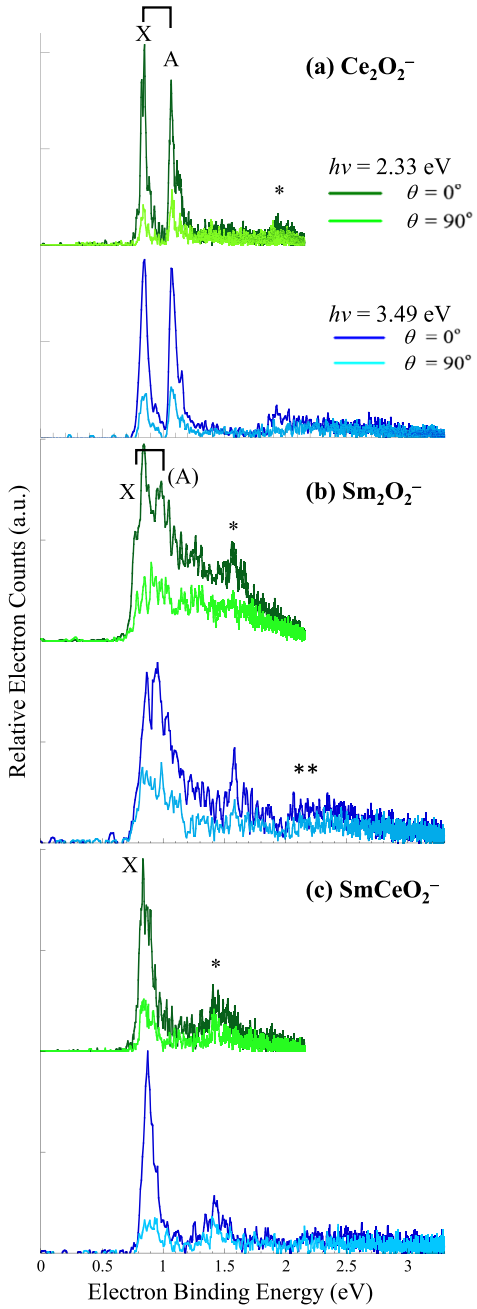

FIG. 8. PE spectra of (a) $Ce_2O_2^-$, (b) $Sm_2O_2^-$, and (c) $SmCeO_2^-$ collected using 2.330 and 3.495 eV photon energies with laser polarizations parallel (dark green and blue traces) and perpendicular (light green and blue traces) to the direction of electron detection. Features indicated with an asterisk (*) are tentatively assigned to shake-up transitions.

TABLE V. Peak positions and tentative assignments for the PE spectra of $Ce_2O_2^-$, $Sm_2O_2^-$, and $SmCeO_2^-$ [Fig. 8]. The values in parentheses represent the uncertainty in the last digit. The uncertainty in the asymmetry parameters is approximately 10%.

	Asymmetry parameter			
	$h\nu$ = 2.33 (eV)	$h\nu$ = 3.49 (eV)	ADE/VDE e^-BE (eV)	Tentative assignment
$Ce_2O_2^-$				
X	1.2	1.2	0.83(2)/0.88(1)	$^3B_{1u} \leftarrow {}^4A_g$
A	0.9	1.0	1.05(2)/1.09(1)	$^5A_g \leftarrow {}^4A_g$
*	...		VDE = 2.3(1)	Shake-up transition
$Sm_2O_2^-$				
X,(A)	1.0	1.0	0.70(1)/0.846(3)	$^{13}A_g \leftarrow {}^{12}A_g$ $^{11}B_{1u} \leftarrow {}^{12}A_g$
*	0.9	0.7	VDE = 1.58(1)	
**	...		VDE = 2.07(1)	
$SmCeO_2^-$				
X	1.0	1.2	0.74(2)/0.834(6)	$^5A_1 \leftarrow {}^6A_1$
*	0.5	0.5	VDE = 1.406(8)	

band X. Additionally, there is considerable continuum signal between bands X and (*) that is more pronounced in the spectrum obtained with 2.330 eV photon energy. As with the photon-energy dependent intensity of band A in the PE spectrum of Sm_2O^-, we consider possible explanations in Sec. IV.

The PE spectrum of $SmCeO_2^-$ is qualitatively similar to the spectrum of Sm_2O_2, with intense band X observed at 0.74(2) eV, and a less intense band labeled with an asterisk (*) at 1.406(8) eV. Overall, the spectrum appears much less congested; band X in the $SmCeO_2^-$ spectrum is slightly broader than the very narrow band X in the $Ce_2O_2^-$ spectrum, and the spectrum obtained using 2.330 eV photon energy exhibits partially resolved features within band X.

The lowest energy structures found computationally for both Sm_2O_2 and $SmCeO_2$ anions and neutrals are four membered rings, as summarized in Figures 9 and 10, respectively, and in Table VI. Diagrams summarizing all the structures in various spin states with their relative energies are included in the supplementary material.

Based on the calculations, $Sm_2O_2^-$ favors a D_{2h} structure. High spin multiplicities resulting from ferromagnetic coupling between the 4*f* electrons localized on the two Sm centers were calculated to be lower in energy than the AF-coupled states. The lowest energy anion predicted computationally is a $^{12}A_g$ state, qualitatively with the $[4f_a^5\,4f_b^5](\sigma_{6s})^2(\sigma_{6s}^*)$ orbital occupancy, where the σ_{6s} and σ_{6s}^* orbitals are similar in nature to the identically labeled Sm_2O^-/Sm_2O orbitals. The σ_{6s}^* orbital appears to have some hybridization with a 4*f* orbital. The most energetically competitive state of $Sm_2O_2^-$ also has the $[4f_a^5\,4f_b^5](\sigma_{6s})^2(\sigma_{6s}^*)$ orbital occupancy, with the σ_{6s}^* electron spin being antiparallel to the electrons in the 4*f* subshell, though this is calculated to be 0.35 eV higher in energy. This $^{10}A_g$ state is of more likely to be ca. 0.05–0.1 eV higher in energy based on weak coupling between the electrons in the core-like 4*f* orbitals and the diffuse HOMO. For example, in the low-lying states of SmO, the analogous high spin-low spin splitting is 415 cm^{-1} and 880 cm^{-1} for the lowest lying states. It is therefore conceivable that transitions from the $^{10}A_g$ state of the anion overlap with transitions from the $^{12}A_g$ state, further congesting the spectrum.

Two neutral states that are one-electron accessible from the $^{12}A_g$ anion (nominally via detachment of the "blue" and

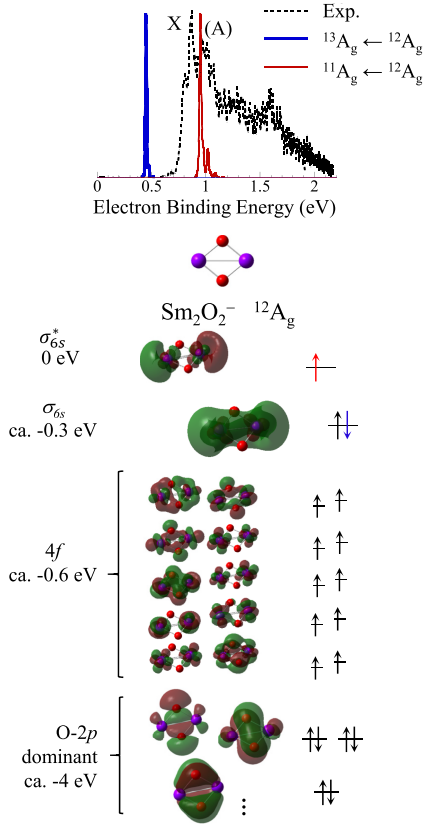

FIG. 9. Summary of the lowest energy structure and spin state that converged in calculations on $Sm_2O_2^-$ and Sm_2O_2, along with the orbital occupancy of the lowest energy state found for $Sm_2O_2^-$. Simulations (solid blue and red traces) of the $Sm_2O_2^-$ PE spectrum (dashed black trace). The simulations are color-coordinated with the detached electrons.

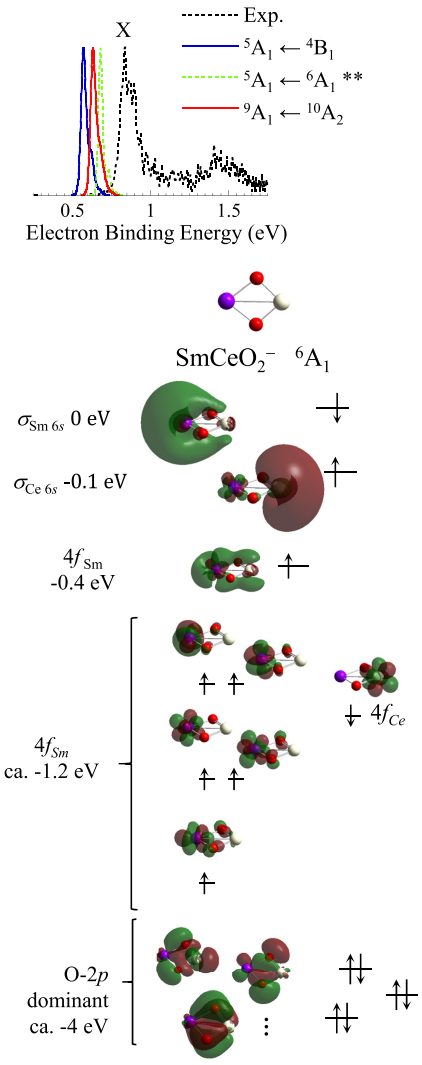

FIG. 10. Summary of the lowest energy structure and spin state that converged in calculations on $SmCeO_2^-$ and $SmCeO_2$, along with the orbital occupancy of the lowest energy state found for $SmCeO_2^-$. Simulations (solid and dashed color traces) of the $SmCeO_2^-$ PE spectrum (dashed black trace). See text for details on dashed color simulation assignment.

"red" electrons in Fig. 9) were calculated with binding energies of 0.45 eV and 0.95 eV, as summarized in Table VI. Simulations based on these calculated structures are nearly vertical, as shown in Fig. 9, and the value of the lowest transition energy deviates from the experimental values more than other calculated transition energies in such a way that it is consistent with the systematic over stabilization of higher spin states by the computational method used.[49] However, we again point out that there will be numerous close-lying $Sm_2O_2^-$ states arising from a common $[4f_a^5 4f_b^5](\sigma_{6s})^2(\sigma_{6s}^*)$ superconfiguration, and the PE spectrum of SmO^- illustrates how the transitions from the various initial anion states to the one-electron accessible neutral states vary in energy. We therefore assign band X to overlapping clusters of transitions associated with the $^{13}A_g$–$^{12}A_g$ and $^{11}B_{1u}$–$^{12}A_g$ transitions.

At first glance, the structures predicted for $SmCeO_2^-$ and $SmCeO_2$ suggest an analogous electronic structure to Ce_2O_2 and Sm_2O_2 anions and neutrals, but a survey of the predicted orbital occupancy shows that the Sm center has nominally a $4f^6$ subshell occupancy, again resulting in longer Sm–O bondlengths compared to Sm_2O_2 (Table IV). The lowest energy $^6A_1$ state found for $CeSmO_2^-$ has a $[4f^6_{Sm}4f_{Ce}](6s_{Ce})(6s_{Sm})$ orbital occupancy, illustrated in Figure 10. As with $SmCeO^-$, for this state, the orbitals appear very localized on the two centers, though they are calculated to be nearly degenerate. Results on several of the other spin states yielded more covalent style with the σ_{6s} and σ^*_{6s} description being more appropriate, as reflected in Table IV. Based on the spin–orbital occupancies, only two transitions from the low-lying electronic states of the anion are allowed to the various neutral states. Herein there lies an example of relying on these calculations to gain more detailed insight into the electronic structures. Nonetheless, simulations on the two allowed transitions based on the spin in the $4f_{Sm}$, $4f_{Ce}$, and $6s$-based MOs, though not necessarily the specific 4f orbitals that are occupied [$^5A_1$–$^4B_1$ and $^9A_1$–$^{10}A_2$], reflect the very small structure change between the anion and neutral. These two simulations are shown as solid traces in Fig. 10. The not-strictly allowed transition between the $^6A_1$ anion and $^5A_1$ neutral ground states predicted computationally is shown as a dashed line. All three simulated transitions are very close in energy and have nearly identical profiles and are similar in appearance to band X in the experimental spectrum.

IV. DISCUSSION

A. Sm 4*f* subshell occupancy

The chemistry of the lanthanoids is similar because the $4f$ orbital occupancy increases incrementally with atomic number across the lanthanoid row in the periodic table. Because the $4f$ orbitals are contracted, the nuclear shielding simply increases to counteract the increase in nuclear charge, and because the $4f$ orbitals do not offer orbital overlap in forming new bonds, the chemistry of these species tends to be governed by the remaining and unchanging number of electrons occupying $5d$, $6s$, and $6p$ orbitals. In the Ln_2O_3 sequioxide materials favored by most lanthanoids [CeO_2 is more stable than Ce_2O_3; europium favors a mixed Eu(II, III) oxide over Eu_2O_3], the partially filled $4f$ band generally lies within the conventional band gaps.[50–54] For Ce_2O_3, each Ce center has a singly occupied $4f$ orbital, and Sm_2O_3 has a $4f^5$ occupancy (the atomic number of Sm is 62, the atomic number of Ce is 58). However, the trend from Ce_2O_3 to Sm_2O_3 is that the bulk $4f$ band energy moves closer to the valence band, and in the case of Sm_2O_3, the $4f$ band energy lies very near the valence band.[47,48] The main finding of this current study is that the $4f^6$ subshell occupancy is competitive in SmO and SmO^-, though the $4f^5$ subshell occupancy is clearly favored for the anion. The $4f^6$ subshell occupancy is *favored* for the less oxidized Sm centers in both Sm_2O and SmCeO anions and neutrals and is favored in the heteronuclear $SmCeO_2$ anion and neutral, while the homonuclear Sm_2O_2 anion and neutral congeners favor the $4f^5$ subshell occupancy.

The implication of these species characterized by $4f^6$ occupancy is that the $4f$ orbitals are sufficiently low in energy that orbital occupancy shifts from the $6s$-based MOs to a $4f$ orbital, which can occur simply because the $4f$ subshell in Sm is lower in energy, comparable to the Sm–O $2p$-dominated

TABLE VI. Summary of results of DFT calculations on the molecular and electronic structures of $Sm_2O_2/Sm_2O_2^-$ and $SmCeO_2/SmCeO_2^-$ including bondlengths, angles, and totally symmetric mode vibrational frequencies. A more extensive catalog of computational results is included in the supplementary material.

Electronic state	Relative energy (eV)	Super-configuration	Allowed transitions	Symmetric mode frequency (cm^{-1})	Sm–O (Å)// ∠(Sm–O–Sm) (deg)
Sm_2O_2				Ring distortion/sym str	
^9A_g	2.12	$4f^{10}\,\sigma_{6s}\sigma^*_{6s}$	$^9A_g \leftarrow {}^{10}A_g$ (1.77 eV)	215/594	2.061//102°
$^{11}B_{1u}$	0.95	$4f^{10}\,\sigma^2_{6s}$	$^{11}A_g \leftarrow {}^{12}A_g$ (0.95 eV); $^{11}B_{1u} \leftarrow {}^{10}A_g$ (0.60 eV)	200/552	2.089//99°
$^{13}A_g$	0.45	$4f^{10}\,\sigma_{6s}\sigma^*_{6s}$	$^{13}A_g \leftarrow {}^{12}A_g$ (0.45 eV)	195/510	2.119//99°
$Sm_2O_2^-$					
$^{10}A_g$	0.35	$4f^{10}\,\sigma^2_{6s}\sigma^*_{6s}$		199/530	2.102//99°
$^{12}A_g$	0	$4f^{10}\,\sigma^2_{6s}\sigma^*_{6s}$		194/508	2.112//99°
$SmCeO_2$				Ring distortion/Sm–O str/Ce–O str	M–O (Sm/Ce)/Å//∠(Sm–O–Ce)
$^7B_1$	0.70	$4f^6_{Sm}\,4f_{Ce}\sigma_{6s}$		200/416/579	2.190/2.046//100°
$^9A_1$	0.69	$4f^6_{Sm}\,4f_{Ce}\sigma_{6s}$	$^9A_1 \leftarrow {}^{10}A_2$ (0.63 eV)	192/396/580	2.233/2.033//100°
$^5A_1$	0.68	$4f^6_{Sm}\,4f_{Ce}\sigma_{6s}$	$^5A_1 \leftarrow {}^4B_1$ (0.57 eV)	201/424/582	2.186/2.051//100°
$SmCeO_2^-$					
$^8A_2$	0.12	$4f^6_{Sm}\,4f_{Ce}6s_{Ce}6s_{Sm}$		185/393/598	2.252/2.042//100°
$^4B_1$	0.11	$4f^6_{Sm}\,4f_{Ce}\sigma_{6s}\sigma^*_{6s}$		191/427/618	2.232/2.044//101°
$^{10}A_2$	0.06	$4f^6_{Sm}\,4f_{Ce}\sigma_{6s}\sigma^*_{6s}$		187/441/631	2.283/2.033//100°
$^6A_1$	0	$4f^6_{Sm}\,4f_{Ce}6s_{Ce}6s_{Sm}$		189/399/598	2.221/2.044//100°

bonding orbitals. The O 2*p*-dominated bonding orbitals, of course, correlate to the bulk valence band in metal oxides.

Considering the Sm centers in SmO, Sm_2O_2, and $SmCeO_2$, which are nominally in the +2 oxidation state, the higher Sm 4*f* subshell occupancy in $SmCeO_2$ suggests that the orbital energy landscape created by the heteronuclear combination tips the balance of $4f^5$ subshell occupancy to $4f^6$ subshell occupancy. The result is weaker Sm–O bonds due to enhanced Sm nuclear shielding. The ionic conductivity of ceria is enhanced when doped with samarium. We suggest that this enhancement may be due to the energetic accessibility of the bond-weakening $4f^6$ subshell occupancy of Sm.

B. Enhancement of intensity of transitions to excited states

The PE spectrum of Sm_2O^- shows a striking photon-energy dependent intensity of a transition to an excited state, with the relative intensity being higher with lower photon energy. Based on comparison with the computational results, the transition involves detachment of the electron from the singly occupied HOMO. In addition, the continuum that congests the PE spectrum of $Sm_2O_2^-$ is also enhanced at a lower photon energy. Threshold effects would have the opposite effect of what is observed. We have previously observed enhancements in photodetachment transitions associated with temporary anion states at e^-KE values that are resonant with the temporary anion state, but they have exhibited isotropic photoelectron angular distributions,[55] in contrast with what is observed in the $Sm_2O_y^-$ ($y = 1, 2$) spectra. We therefore consider two other potential explanations for this phenomenon.

First, the 6*s*, 5*d*, and 6*p* atomic orbitals in the lanthanides are energetically close, which results in numerous low-lying electronic excitations that could potentially be (1) at term energies of 2.33 eV above the ground state of the anion and (2) correlate only to the Sm_2O_y excited state. A hypothetical example is the dipole allowed excitation of the electron in the Sm_2O^- HOMO to the LUMO + 2, depicted in Fig. 6. Since this excited state (hypothetically), 2.33 eV above the anion ground state, is not bound with respect to the detachment continuum, the excited state would autodetach. There are no one-electron autodetachment transitions that would lead to the neutral ground electronic state, whereas electron autodetachment from the excited state HOMO would leave the neutral in the first excited state, with e^-KE values identical to those resulting from direct detachment. On the other hand, the enhancement of continuum signal in the $Sm_2O_2^-$ spectrum does not seem as readily explained by autodetachment from a quasibound excited anion state.

A second explanation could be interactions between the photoelectrons and the large magnetic moment of the high-spin Sm_2O_y neutral partner resulting from high spin, $|\boldsymbol{J}_1\rangle$ states. As the photoelectron moves away, the remnant neutral adapts in a manner so as to conserve the total angular momentum of the (neutral + photoelectron) system. Hence, $|\boldsymbol{J}_1\rangle$ becomes time-dependent, and therefore e^-KE dependent. In the limit of high photon energy, the electron and neutral partner interact over a short period of time, that is, the period required for the photoelectron to escape the high interaction region originating from the neutral species. Therefore, the experimental observable (electron momentum, or e^-KE) will reflect, in this case, the electronic structure of the source anion at the time of the (sudden) detachment. For lower photon energies,

the photoelectron, which has time-dependent orbital and spin angular momentum as it travels away from the neutral with finite momentum, i.e., $|\boldsymbol{J}_2\rangle \cdot e^{-ik(t)x}$, interacts over a longer period of time with the neutral partner, $|\boldsymbol{J}_1\rangle$. As the electron moves away, the neutral adapts in a manner so as to again conserve total angular momentum and the neutral state is retained in a coherent superposition of the multiple pure-$\boldsymbol{J}_1$ states that are accessible to the neutral over narrow energy windows. There are numerous close-lying spin states arising from the $4f^5$ or $4f^6$ subshell occupancy in the samarium oxide species relative to the cerium oxide species, a sampling of which are shown in the supplementary material (Figures S5 and S7) and these states assist in the construction of the coherent superposition state. These states may be populated during the dynamical process of photoelectron detachment described above, which will have a greater effect for slower electrons, since the slower photoelectrons allow a greater mixing of these pure-$\boldsymbol{J}_1$ states by extending the time of interaction and perturbation of the neutral due to the outgoing photoelectron, leading to more intense excited state bands in spectra measured with lower photon energies. Note further that since only an orbital angular momentum of $\ell = 1$ is observed for the outgoing photoelectron, based on the photoelectron angular distributions, this corresponds to a total angular momentum of $j = 3/2$ and 1/2, implying very specific selection rules for population of angular momentum states of the remnant neutral. We are currently looking into this effect in more detail.

V. CONCLUSIONS

A systematic study of small homo- and heteronuclear Sm–Ce suboxide molecules using anion PE spectroscopy is supported by a qualitative interpretation of the results of density functional theory (DFT) calculations. In contrast with the simple PE spectrum of CeO^- measured previously,[37] the PE spectrum of SmO^- exhibits overlapping transitions between three anion states arising from Sm $J_a = 2.5$, $J_a = 2.5$, $\Omega = J_a - 1, 2, 3$ to five neutral states, also arising from $J_a = 2.5$. From the known neutral state energies, we are able to determine the relative energies of the three initial anion states, which lie within a 250 cm^{-1} window of energy. The EA of SmO is 1.067(6) eV. This EA value is within the fairly narrow range of EAs of a wide range of other *LnO* diatomics and larger cerium oxide clusters studied previously,[38] for which we have determined that the transition involves detachment from a molecular orbital with a strong Ln 6*s* character.

The unique finding of this study involves the occupancy of the contracted 4*f* subshell of the Sm centers in these oxo species. While the Sm center in SmO and Sm_2O_2 anions and neutrals favor the ligand field-stabilized $4f^5$ 6*s* superconfiguration, the Sm center in the $SmCeO_2$ neutral appears to favor a $4f^6$ superconfiguration, resulting in weaker Sm–O bonds relative to the Ce–O bonds. The Ce center superconfiguration in all of these related species maintains the analogous ligand field-stabilized $4f^{(1)}$ subshell occupancy. In the less oxidized Sm_2O and SmCeO molecules, the $4f^6$ 6*s* superconfigurations are favored. These results show that the Sm $4f^5$ and $4f^6$ subshell occupancies are energetically competitive, but in the +2 oxidation state that favors the $4f^5$ 6*s* superconfiguration in the homonuclear Sm_xO_x species, the combination of Ce and Sm drives the $4f^6$ subshell occupancy on Sm. The result is a weakened Sm–O bond.

Unusual lower photon energy enhancement of an excited state transition in the spectrum of Sm_2O^- and the enhancement of continuum signal in the spectrum of $Sm_2O_2^-$ were discussed. We considered the possibility of transitions to excited anion states that subsequently undergo autodetachment, as well as e^-KE-dependent interactions between the outgoing photoelectron and the magnetic moment of the high-spin neutral final state. This effect will be the subject of further study, since similar effects have been observed in several of the tri-metallic heteronuclear Sm–Ce oxides.

SUPPLEMENTARY MATERIAL

See supplementary material for details on spectroscopic parameters used to generate PE spectral simulations, diagrams showing all structures and energies that converged in calculations, and a complete list of Cartesian coordinates and total energies for all structures that converged in the calculations.

ACKNOWLEDGMENTS

This work was supported by National Science Foundation Grant No. CHE-1265991.

[1] D. R. Mullins, Surf. Sci. Rep. **70**, 42 (2015).
[2] R. J. Gorte, AIChE J. **56**, 1126 (2010).
[3] A. Bruix, J. A. Rodriguez, P. J. Ramírez, S. D. Senanayake, J. Evans, J. B. Park, D. Stacchiola, P. Liu, J. Hrbek, and F. Illas, J. Am. Chem. Soc. **134**, 8968 (2012).
[4] E. S. Bickford, S. Velu, and C. Song, Prepr. Pap.-Am. Chem. Soc., Div. Fuel Chem. **48**, 810 (2003).
[5] T. Bunluesin, R. J. Gorte, and G. W. Graham, Appl. Catal., B **15**, 107 (1998).
[6] A. Luengnaruemitchai, S. Osuwan, and E. Gulari, Catal. Commun. **4**, 215 (2003).
[7] Y. Li, Q. Fu, and M. Flytzani-Stephanopoulos, Appl. Catal., B **27**, 179 (2000).
[8] J. Vecchietti, A. Bonivardi, W. Xu, D. Stacchiola, J. J. Delgado, M. Calatayud, and S. E. Collins, ACS Catal. **4**, 2088 (2014).
[9] S. Hui, J. Roller, S. Yick, X. Zhang, C. Decès-Petit, Y. Xie, R. Maric, and D. Ghosh, J. Power Sources **172**, 493 (2007).
[10] H. Inaba and H. Tagawa, Solid State Ionics **83**, 1 (1996).
[11] F. Y. Wang, S. Chen, and S. Cheng, Electrochem. Commun. **6**, 743 (2004).
[12] S. Zha, C. Xia, and G. Meng, J. Power Sources **115**, 44 (2003).
[13] J. Huang, L. Yang, R. Gao, Z. Mao, and C. Wang, Electrochem. Commun. **8**, 785 (2006).
[14] K. Eguchi, T. Setoguchi, T. Inoue, and H. Arai, Solid State Ionics **52**, 165 (1992).
[15] S. M. Haile, Acta Mater. **51**, 5981 (2003).
[16] S. Kuharuangrong, J. Power Sources **171**, 506 (2007).
[17] G. B. Balazs and R. S. Glass, Solid State Ionics **76**, 155 (1995).
[18] W. Huang, P. Shuk, and M. Greenblatt, Solid State Ionics **100**, 23 (1997).
[19] J. Huang, Z. Mao, Z. Liu, and C. Wang, Electrochem. Commun. **9**, 2601 (2007).
[20] C. Xia, Y. Li, Y. Tian, Q. Liu, Z. Wang, L. Jia, Y. Zhao, and Y. Li, J. Power Sources **195**, 3149 (2010).
[21] H. Yahiro, Y. Eguchi, K. Eguchi, and H. Arai, J. Appl. Electrochem. **18**, 527 (1988).
[22] T. Kudo and H. Obayashi, J. Electrochem. Soc. **123**, 415 (1976).
[23] H. L. Tuller and A. S. Nowick, J. Electrochem. Soc. **122**, 255 (1975).
[24] J. W. Fergus, J. Power Sources **162**, 30 (2006).
[25] V. V. Kharton, F. M. B. Marques, and A. Atkinson, Solid State Ionics **174**, 135 (2004).
[26] S. M. Lang and T. M. Bernhardt, Phys. Chem. Chem. Phys. **14**, 9255 (2012).

[27]J. E. Mann, N. J. Mayhall, and C. C. Jarrold, Chem. Phys. Lett. **525-526**, 1 (2012).
[28]Y. Suchorski, R. Wrobel, S. Becker, and H. Weiss, J. Phys. Chem. C **112**, 20012 (2008).
[29]F. Yang, J. Graciani, J. Evans, P. Liu, J. Hrbek, J. F. Sanz, and J. A. Rodriguez, J. Am. Chem. Soc. **133**, 3444 (2011).
[30]S. D. Senanayake, P. J. Ramírez, I. Waluyo, S. Kundu, K. Mudiyanselage, Z. Liu, Z. Liu, S. Axnanda, D. J. Stacchiola, J. Evans, and J. A. Rodriguez, J. Phys. Chem. C **120**, 1778 (2016).
[31]Z. Liu, D. C. Grinter, P. G. Lustemberg, T.-D. Nguyen-Phan, Y. Zhou, S. Luo, I. Waluyo, E. J. Crumlin, D. J. Stacchiola, J. Zhou, J. Carrasco, H. F. Busnengo, M. V. Ganduglia-Pirovano, S. D. Senanayake, and J. A. Rodriguez, Angew. Chem., Int. Ed. **55**, 7455 (2016).
[32]P. G. Lustemberg, P. J. Ramírez, Z. Liu, R. A. Gutiérrez, D. G. Grinter, J. Carrasco, S. D. Senanayake, J. A. Rodriguez, and M. V. Ganduglia-Pirovano, ACS Catal. **6**, 8184 (2016).
[33]J. A. Rodriguez, D. C. Grinter, Z. Liu, R. M. Palomino, and S. D. Senanayake, Chem. Soc. Rev. **46**, 1824 (2017).
[34]G. Pacchioni, Phys. Chem. Chem. Phys. **15**, 1737 (2013).
[35]J. Paier, C. Penschke, and J. Sauer, Chem. Rev. **113**, 3949 (2013).
[36]J. Carrasco, D. López-Durán, Z. Liu, T. Duchoň, J. Evans, S. D. Senanayake, E. J. Crumlin, V. Matolin, J. A. Rodriguez, and M. V. Ganduglia-Pirovano, Angew. Chem., Int. Ed. **54**, 3917 (2015).
[37]M. Ray, J. Felton, J. O. Kafader, J. E. Topolski, and C. C. Jarrold, J. Chem. Phys. **142**, 064305 (2015).
[38]J. O. Kafader, J. E. Topolski, and C. C. Jarrold, J. Chem. Phys. **145**, 154306 (2016).
[39]R. W. Field, Ber. Bunsenges. Phys. Chem. **86**, 771 (1982).
[40]V. D. Moravec and C. C. Jarrold, J. Chem. Phys. **108**, 1804 (1998).
[41]S. E. Waller, J. E. Mann, and C. C. Jarrold, J. Phys. Chem. A **117**, 1765 (2013).
[42]M. J. Frisch, G. W. Trucks, H. B. Schlegel, G. E. Scuseria, M. A. Robb, J. R. Cheeseman, G. Scalmani, V. Barone, B. Mennucci , G. A. Petersson, H. Nakatsuji, M. Caricato, X. Li, H. P. Hratchian, A. F. Izmaylov, J. Bloino, G. Zheng, J. L. Sonnenberg, M. Hada, M. Ehara, K. Toyota, R. Fukuda, J. Hasegawa, M. Ishida, T. Nakajima, Y. Honda, O. Kitao, H. Nakai, T. Vreven, J. A. Montgomery, Jr., J. E. Peralta, F. Ogliaro, M. J. Bearpark, J. Heyd, E. N. Brothers, K. N. Kudin, V. N. Staroverov, R. Kobayashi, J. Normand, K. Raghavachari, A. P. Rendell, J. C. Burant, S. S. Iyengar, J. Tomasi, M. Cossi, N. Rega, N. J. Millam, M. Klene, J. E. Knox, J. B. Cross, V. Bakken, C. Adamo, J. Jaramillo, R. Gomperts, R. E. Stratmann, O. Yazyev, A. J. Austin, R. Cammi, C. Pomelli, J. W. Ochterski, R. L. Martin, K. Morokuma, V. G. Zakrzewski, G. A. Voth, P. Salvador, J. J. Dannenberg, S. Dapprich, A. D. Daniels, Ö. Farkas, J. B. Foresman, J. V. Ortiz, J. Cioslowski, and D. J. Fox, GAUSSIAN 09, Gaussian, Inc., Wallingford, CT, USA, 2009.
[43]X. Cao and M. Dolg, J. Chem. Phys. **115**, 7348 (2001).
[44]P. Carette and A. Hocquet, J. Mol. Spectrosc. **131**, 301 (1988).
[45]C. Linton, G. Bujin, R. S. Rana, and J. A. Gray, J. Mol. Spectrosc. **126**, 370 (1987).
[46]J. O. Kafader, M. Ray, and C. C. Jarrold, J. Chem. Phys. **143**, 064305 (2015).
[47]E. van der Kolk and P. Dorenbos, Chem. Mater. **18**, 3458 (2006).
[48]R. Gillen, S. J. Clark, and J. Robertson, Phys. Rev. B **87**, 125116 (2013).
[49]J. Harvey, "DFT computation of relative spin-state energetics of transition metal compounds," in *Structure and Bonding* (Springer, Berlin, 2004).
[50]J. L. F. Da Silva, M. V. Ganduglia-Pirovano, J. Sauer, V. Bayer, and G. Kresse, Phys. Rev. B **75**, 045121 (2007).
[51]P. J. Hay, R. L. Martin, J. Uddin, and G. E. Scuseria, J. Chem. Phys. **125**, 034712 (2006).
[52]K. T. Jacob and A. Rajput, J. Chem. Eng. Data **61**, 1710 (2016).
[53]K. T. Jacob, A. Dixit, and A. Rajput, Bull. Mater. Sci. **39**, 603 (2016).
[54]J. N. Beukers, J. E. Kleibeuker, G. Koster, D. H. A. Blank, G. Rijnders, H. Hilgenkamp, and A. Brinkman, Thin Solid Films **518**, 5173 (2010).
[55]K. M. Patros, J. E. Mann, and C. C. Jarrold, J. Phys. Chem. A **120**, 7828 (2016).